# Tuning the Structure of Thermosensitive Gold Nanoparticle Monolayers

**Camila A. Rezende,[†] Jun Shan,[‡] Lay-Theng Lee,*[,†] Gilbert Zalczer,[§] and Heikki Tenhu[‡]**

*Laboratoire Léon Brillouin, UMR12, CEA-Saclay, 91191 Gif-sur-Yvette Cedex, France, Laboratory of Polymer Chemistry, University of Helsinki, PB 55, FIN-00014 HY, Finland, and Service de Physique de l'Etat Condensé, URA 2464, CEA-Saclay, 91191 Gif-sur-Yvette Cedex, France*

*Received: February 25, 2009; Revised Manuscript Received: June 9, 2009*

Gold nanoparticles grafted with poly(*N*-isopropylacrylamide) (PNIPAM) are rendered amphiphilic and thermosensitive. When spread on the surface of water, they form stable Langmuir monolayers that exhibit surface plasmon resonance. Using Langmuir balance and contrast-matched neutron reflectivity, the detailed structural properties of these nanocomposite monolayers are revealed. At low surface coverage, the gold nanoparticles are anchored to the interface by an adsorbed PNIPAM layer that forms a thin and compact pancake structure. Upon isothermal compression ($T = 20$ °C), the adsorbed layer thickens with partial desorption of polymer chains to form brush structures. Two distinct polymer conformations thus coexist: an adsorbed conformation that assures stability of the monolayer, and brush structures that dangle in the subphase. An increase in temperature to 30 °C results in contractions of both adsorbed and brush layers with a concomitant decrease in interparticle distance, indicating vertical as well as lateral contractions of the graft polymer layer. The reversibility of this thermal response is also shown by the contraction−expansion of the polymer layers in heating−cooling cycles. The structure of the monolayer can thus be tuned by compression and reversibly by temperature. These compression and thermally induced conformational changes are discussed in relation to optical properties.



## Introduction

Gold nanoparticles have been a subject of much interest for several centuries, dating back to Roman times, where metal nanoparticles were used as decorative pigments. The most famous example showing the intriguing optical properties of these nanoparticles is the Lycurgus Cup[1] (dated fourth to fifth century A.D.), where gold and silver nanoparticles were incorporated into the glass to impart brilliant colors and, more fascinating, to create an optical illusion of changing colors depending on whether it is viewed by transmitted (ruby red) or reflected (yellowish green) light. The scientific report by Michael Faraday,[2] the first known documented systematic study on the optical properties of these metallic colloids, has also provided ground for continued interest in this area theoretically and experimentally. More recently, research has concentrated on very small metal particles[3−7] that exhibit collective oscillation of the conduction-band electrons when irradiated by light. This phenomenon, so-called dipole or surface plasmon resonance (SPR),[5,7] is an important optical signature that, in the case of noble metal nanoparticles, results in absorption in the UV−vis spectrum that gives rise to characteristic bright colors. The factors that govern SPR of individual particles are particle size[8−12] and shape;[12,13] dielectric environment,[13−17] which includes the solvent refractive index and the properties of the stabilizing ligands; and interparticle distance.[12,18−20]

Due to their high specific surface area, nanoparticles often require additional stabilization to prevent aggregation. For this purpose, short-chain organic molecules[14−16] and graft polymer chains[21−24] have been used. In the latter case, gold nanoparticles are grafted with two types of polymers: polystyrene (PS) and poly(*N*-isopropylacrylamide) (PNIPAM). These nanoparticles are thus amphiphilic and can be spread on the water−air interface where the hydrophobic PS acts as an anchor to attach the nanoparticle to the interface while PNIPAM is a water-soluble thermosensitive polymer that undergoes the coil−globule transition at $T \sim 32$ °C. Therefore, when grafted onto nanoparticles, the PNIPAM layer confers colloidal stability and more importantly, by its thermal response, provides a convenient route to modulate interparticle distances. These PS- and PNIPAM-protected gold nanoparticles (PS-PNIPAM-AuNPs) form stable Langmuir monolayers that exhibit SPR in the UV−vis range.[24] Two major observations were reported: a blue-shift of the SPR peak upon isothermal compression of the monolayer and a red-shift with increase in temperature. While the red-shift was attributed to dipole coupling promoted by a decrease in interparticle distance due to thermal collapse of the PNIPAM shell, the blue-shift was however an unexpected result. More recently, gold nanoparticles encapsulated with PNIPAM gel have also been reported to exhibit a significant red-shift when the nanoparticle dispersion is heated above the polymer transition temperature.[25] Thus, when coated with a thermosensitive polymer layer, metallic nanoparticle optical properties can be manipulated by temperature.

Although thermally induced changes in optical properties of PNIPAM-coated nanoparticles are attributed to modifications of the thermosensitive polymer shell layer, a direct study of the structural properties of these composite nanoparticles has never been reported. In this study, we use neutron reflectivity to probe directly the structural properties of amphiphilic PNIPAM-gold nanoparticle Langmuir monolayers. The structures of the graft polymer layer and of the gold core are studied separately using contrast-variation. The conformational changes

* Corresponding author. E-mail: Lay-Theng·Lee@cea.fr.
[†] Laboratoire Léon Brillouin, UMR12, CEA-Saclay.
[‡] University of Helsinki.
[§] Service de Physique de l'Etat Condensé, URA 2464, CEA-Saclay.

10.1021/jp9019393 CCC: $40.75 
Published on Web 07/01/2009

of the polymer layer induced by compression and by temperature are reported with a general discussion of their relation to optical properties.

## Materials and Methods

**Materials.** ***1. Synthesis of cpa-PNIPAM.*** cpa-PNIPAM was synthesized by RAFT polymerization using 4-cyanopentanoic acid dithiobenzoate as RAFT agent. Details of the synthesis routes have been reported in earlier communications.[23,26] Briefly, 6.2 g of NIPAM monomer (2.19 M), 27.0 mg of cpa-RAFT agent (3.87 mM), and 2.0 mg of AIBN (0.49 mM) were dissolved in 25 mL of dioxane in a round-bottom flask equipped with a magnetic stirrer. The mixture was degassed by three freeze−pump−thaw cycles, sealed under vacuum, and polymerized in a thermostated oil bath at 60 °C for 47 h. The polymer was precipitated in an excess of diethyl ether, purified by repeated precipitations, and dried under vacuum. The molar mass was $M_n = 13680$ g/mol with a polydispersity index of 1.17, as measured by size exclusion chromatography.

***2. Synthesis and Characterization of Gold Nanoparticles Protected with cpa-PNIPAM.*** The cpa-PNIPAM-gold nanoparticles (PNIPAM-AuNPs) were prepared in a homogeneous THF phase in a one-pot reaction.[22] The molar ratio of cpa-RAFT-PNIPAM:$HAuCl_4 \cdot xH_2O$ was kept at 1:5. High-resolution transmission electron microscopy (HRTEM) was used to characterize the as-prepared PNIPAM-AuNPs. HRTEM images of the nanoparticles were obtained with a Philips CM200FEG, working at an accelerating voltage of 200 keV. The point-to-point resolution was 0.24 nm. Images were recorded with a GATAN slow scan CCD camera. Samples were prepared by casting one drop of the appropriately diluted nanoparticle solution in methanol onto a carbon film mounted on a copper grid (S147-4, 400 mesh Cu, Agar Scientific Ltd.) and dried in air. The size distribution of gold nanoparticles was measured from the enlarged photographs of the TEM images for at least 200 individual gold core images. The mean size of PNIPAM-AuNP was $d_p = 3.4 \pm 1.1$ nm. The amount of cpa-PNIPAM ligand on the gold core surface was determined by thermogravimetric analysis (TGA, Mettler Toledo TGA 850) in a flowing nitrogen atmosphere. Temperature was increased from 20 to 800 °C at a rate of 10 °C/min. These analyses yield a formula of $PNIPAM_{52}Au_{1289}$.

**Compression Isotherms.** Surface pressure−area ($\pi$−$A$) isotherms were recorded using a Kibron MicroTroughX (Kibron Inc., Finland). The trough area was 108 $cm^2$, and the trough volume was ~22 mL. Millipore water was used as subphase. Au-PNIPAM nanoparticles were dissolved in chloroform, and the dispersion was spread on the water surface with a Hamilton microsyringe. After about 20 min to ensure complete evaporation of the solvent, the surface film was compressed symmetrically at a constant speed of 3 mm/min (156 $mm^2$/min). The surface-pressure isotherms were recorded with a Wilhelmy wire probe. The measurements were conducted at $T = 22 \pm 0.5$ °C and $T = 30 \pm 1.0$ °C.

**Optical Measurements.** Optical absorption measurements of PNIPAM-AuNPs were performed on monolayers spread from chloroform on the surface of Millipore water. The container was a glass cell with a transparent bottom mounted on an antivibration table. Spectra acquisition was made after about 10 min following sample deposition. Light from a halogen bulb transmitted through a 600 $\mu$m core silica fiber and made parallel by a convergent lens was directed from the bottom of the cell across the water interface at normal incidence. It was focused on another fiber above the sample surface and delivered to a multichannel spectrometer (Ocean Optics SD2000). Spectra from pure water and from water spread with pure chloroform were recorded for reference and to verify that any residual chloroform did not affect the absorption spectra in the range of interest. Absorption was evaluated from $1 - I_s/I_w$, where $I_w$ and $I_s$ are the intensities of transmitted light in pure water and in the presence of a monolayer, respectively. The surface coverage of the nanoparticles was increased by spreading incremental volumes of the sample. The temperature around the sample was controlled at $T = 22 \pm 0.5$ °C.

**Neutron Reflectivity Measurements.** Specular reflectivity from an ideal interface (bare surface in the absence of an adsorbed layer) is referred to as the Fresnel reflectivity, $R_F$. It is defined as[27]

$$R_F(k) = \left[\frac{(k_0 - k_i)}{(k_0 + k_i)}\right]^2$$

where $k_0 = (2\pi/\lambda) \sin\theta$ and $k_i = (k_0^2 - 4\pi Nb)^{1/2}$ are the wave vectors outside and inside the medium, respectively, $\lambda$ is the neutron wavelength and $\theta$ is the grazing incident angle. Alternatively, in the kinematic approximation, it can be expressed as[28]

$$R_F(k) = \frac{\pi^2}{k^4}|\Delta\rho|^2$$

where $\Delta\rho$ is difference in scattering length density across the interface. It can be seen from this expression that the reflectivity decreases asymptotically with $k^{-4}$. In the presence of a surface layer, the reflectivity deviates from $R_F$ and this deviation can be related to the Fresnel reflectivity by

$$\frac{R(k)}{R_F(k)} = \left(\int \rho'(z) \exp(2ikz)\, dz\right)^2$$

where $\rho(z)'$ is the gradient of the scattering length density and

$$\frac{R(k)}{R_F(k)} = \left(\int \frac{d(Nb)}{dz} \exp(2ikz)\, dz\right)^2$$

Nb is the scattering length density that is related to the chemical composition of the adsorbed layer. Thus, when the reflectivity is represented in this reduced form, all deviations of $R/R_F$ from unity are due only to interfacial features such as roughness and adsorbed layers. When $R_F$ is convoluted with instrumental resolutions and surface roughness of the pure substrate, $R/R_F$ is then attributed directly to the composition profile of the adsorbed layer. In this paper, all reflectivity data are represented in this normalized form.

Neutron reflectivity experiments were carried out on the time-of-flight neutron reflectometer EROS (Laboratoire Léon Brillouin, CEA-Saclay, France) where a horizontal polychromatic beam (wavelengths range from 2.5 to 25 Å) was bent to the required incident angle onto the liquid surface using a supermirror. The sample container was a Teflon cell (15.0 × 5.0 $cm^2$) that was enclosed in an airtight aluminum cell with quartz windows to allow the neutron beam to pass through with minimal absorption. We chose to use this smaller cell setup instead of the compression trough for neutron reflectivity measurements for two major reasons. First, the large volume

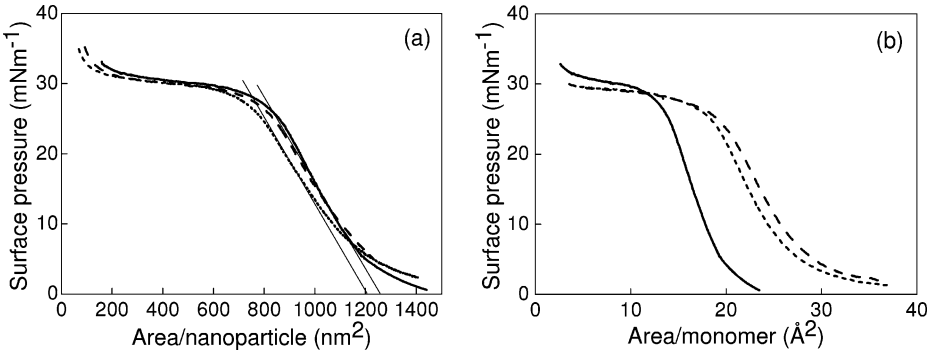


**Figure 1.** (a) Compression isotherms of PNIPAM-AuNPs at $T \approx 22$ °C (solid and dashed lines) and at $T \approx 30$ °C (dotted line). (b) Comparison with PNIPAM homopolymers plotted versus area/NIPAM monomer: PNIPAM-AuNPs (solid line); PNIPAM homopolymers, $M_w = 90$ K (dotted line); and $M_w = 190$K (dashed line).



of free space in the compression trough results in significant exchange of $H_2O$ from the air with the $D_2O$ subphase, an event that results in a continual change in the scattering length density of the subphase during the spectra acquisition. This exchange is minimal using the small airtight cell, and the bulk scattering length density remains constant even after several days. Second, the smaller cell was equipped with a temperature control system that allows the sample temperature to be monitored to ±0.1 °C. In this setup, the surface concentration of PNIPAM-AuNPs nanoparticles was increased by spreading an incremental amount of the nanoparticles dissolved in chloroform. We have found from past[29,30] and present studies that, using this incremental method (varying amount deposited on fixed area), the surface pressure was within ±15% of that registered using a compression trough (fixed amount deposited on varying area). The final surface concentration of material deduced by neutron reflectivity is about 80−85% of the actual amount deposited, indicating an acceptable spreading efficiency.

Two series of experiments were conducted using aqueous subphases of different isotopic compositions: (i) a mixture of $D_2O$ and $H_2O$ (20:80 volume fraction) to contrast-match out the polymer in order to study the structure of the gold core and (ii) pure $D_2O$ to study the polymer structure. The grazing incident angles used for the two series of experiments were 0.63° ± 0.05 and 1.87° ± 0.04, respectively, giving total reflection at a critical wavelength around 22 Å.

## Results

**Compression Isotherms.** The surface pressure versus area ($\pi$−$A$) isotherms of spread PNIPAM-AuNPs are given in Figure 1a. For compression at $T \approx 22$ °C, curves obtained with different initial deposited amounts, ∼8 μL (solid line) and ∼14 μL (dashed line), of the dispersion are also shown. It can be seen that the curves show similar features classically observed for compressed polymer layers. Two characteristic regions can be identified: an initial slow pressure rise region ascribed to 2-D segment interactions, the so-called "pancake" region,[31] followed by a pseudoplateau region with $\pi \sim 30$ mN m$^{-1}$, a value that is close to the saturation pressure of adsorbed PNIPAM.[32] The interfacial behavior of the nanoparticle monolayer is thus dominated by the polymer chains; this is reasonable considering the larger size of the grafted polymer chain ($R_g \approx 4$ nm evaluated based on a free unattached chain) compared to the gold core ($r_p = 1.7$ nm). Extrapolation of the pancake region of the isotherm to $\pi = 0$ yields the pancake limiting area, $A_p \approx$ 1250 nm$^2$ per nanoparticle (gold core + polymer shell layer). The plateau region is generally attributed to desorption of polymer segments into the bulk phase when steric repulsion exceeds the adsorption energy. At $T \approx 30$ °C, the compression curve is very similar, with an apparent decrease in the pancake limiting area to $A_p \approx 1200$ nm$^2$ per nanoparticle, although this small change is close to the experimental uncertainty of these experiments. Beyond the pseudoplateau region, a second pressure rise is obtained at both temperatures.

Figure 1b shows a comparison of the compression isotherms for PNIPAM-AuNPs and PNIPAM homopolymers of different chain lengths, $M_w = 90$ K and 190 K. We point out that, for these "adsorbed" systems (as opposed to "tethered" systems using hydrophobic anchoring blocks), the compression isotherms can be sensitive to compression rate and the initial volume of sample deposited. All the isotherms are therefore registered at the same compression rate of 3 mm/min and with equivalent initial amount of sample (except curves in Figure 1a where solid and dashed lines compare different initial amounts deposited). In Figure 1b, the surface concentration is normalized to the total number of monomers per chain (or per nanoparticle) and plotted versus area/monomer. For the two homopolymers, the curves superpose quite well; the small shift in the slow-pressure rise region could be due to chain length polydispersity or to error in spreading efficiency of the monolayer from the chloroform solution. Nevertheless, both the onset and height of the pseudoplateau are independent of polymer chain length, as expected. Extrapolation of the pancake region of the isotherm to $\pi = 0$ yields the pancake limiting area, $A \approx 28.5$ Å$^2$ per monomer.

For the PNIPAM-AuNP however, the curve does not superpose with those of the homopolymer. The shift to smaller area per unit NIPAM might at first sight suggest loss of material due to desorption into the bulk phase. However, different compression−expansion cycles give reproducible results within experimental error and with typical small hysteresis; loss of material therefore does not seem to be the cause of the shift. A more plausible reason for the low-pressure shift is an overestimation of surface coverage by the grafted polymer chains. Here, for the normalization to area/monomer, we have taken into account all of the monomers on the nanoparticle; $M$ = number of monomers per chain × number of chains per nanoparticle. This clearly overevaluates the total number of monomers per particle that occupies the surface in a 2-D pancake configuration. In order to superpose this pancake region of the curve with that of the homopolymer, it is necessary to multiply $M$ by a factor of about 0.7.

In the pseudoplateau region, PNIPAM-AuNP also shows notable differences compared to the homopolymers. First, the PNIPAM-AuNP curve shows a gradual rise in pressure that is more marked, suggesting a higher degree of conformational

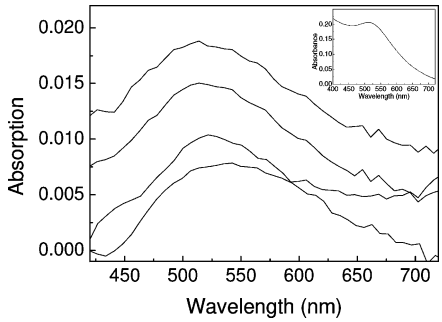


**Figure 2.** Absorption of PNIPAM-AuNP monolayers. Surface coverage increases from the bottom ($a \approx 500$ nm$^2$ per nanoparticle) to the top ($a \approx 100$ nm$^2$ per nanoparticle); $T \approx 22$ °C. The inset shows the absorption peak in bulk water.

changes with compression in this region. Second, a second pressure rise occurs at about $A_b \approx 200-300$ nm$^2$ per nanoparticle, indicative of a pancake−brush transition; this feature is absent for homopolymers.

**Optical Measurements.** The PNIPAM-AuNP monolayers exhibit SPR in the UV−vis range. Figure 2 shows the absorption spectra of the monolayer in the range of surface concentration from $a \approx 500$ nm$^2$ to $a \approx 100$ nm$^2$ per nanoparticle. The intensities are relatively low due to the small particle size ($d_p \approx 3.4$ nm) and to the relatively low surface concentrations. Nevertheless, the plasmon absorption peaks can be seen and the intensity increases with increase in surface concentration.

**Neutron Reflectivity Measurements.** Neutron reflectivity provides direct access to structural information of the PNIPAM-AuNP monolayers. Two different contrast schemes are used to probe separately the structures of the gold core and of the graft polymer layer.

***1. Gold-Core Reflectivity.*** In this series of experiments, the polymer is contrast-matched to the solvent and only the gold core contributes to the excess reflectivity signal. The solvent consists of a mixture of $H_2O$ and $D_2O$ (80:20 by volume) with a scattering length density $Nb_s = 0.82 \times 10^{-6}$ Å$^{-2}$, matching that of PNIPAM considering 20% exchangeable labile H with D. The excellent contrast-match condition is confirmed by the superposition of the reflectivity curves for pure solvent and for a solution containing adsorbed PNIPAM homopolymer chains (in the absence of gold nanoparticles). Figure 3a shows normalized reflectivity, $R/R_F$, for PNIPAM-AuNPs spread on the surface of polymer-contrast-matched water at different surface concentrations at $T = 20$ °C. $R_F$ is the reflectivity of the pure solvent, taking into consideration angular resolution. In this normalized representation, since the polymer is contrast-matched to solvent, all deviations of $R/R_F$ from unity are attributed only to the gold-core layer. The contrast (difference in scattering length density of adsorbed layer and solvent) in this case is positive, $\Delta Nb = Nb_{gc} - Nb_s = (4.50 - 0.82) \times 10^{-6}$ Å$^{-2}$ $= +3.68 \times 10^{-6}$ Å$^{-2}$, where $Nb_{gc}$ is the scattering length density of the gold core, and the normalized reflectivity therefore gives $R/R_F > 1$.

The different curves in Figure 3 are separated vertically for better visualization. The solid lines through the experimental points are best-fit curves calculated using a one-layer model with the corresponding profile shown in Figure 3b. This model describes adequately the gold nanoparticle interfacial layer with two fitting parameters: thickness $d$ and volume fraction of the gold-core $\phi_{gc}$ with a Gaussian error-function roughness $\sigma = 3$ Å at each interface. It is found that increasing the density profile to a two-layer model does not improve the goodness of fit, giving $\chi^2 = 1.128$ compared to $\chi^2 = 1.106$ for a one-layer model (at surface coverage $a \approx 200$ nm$^2$ at $T = 20$ °C).

It can be seen that, with an increase in surface coverage, the volume fraction of the gold core increases while the thickness of the layer remains almost constant around 33 Å. The thickness of the layer measured here thus corresponds closely to the diameter of the gold-core evaluated by TEM ($d_p = 3.4$). The volume fraction of the gold core in the monolayer layer is evaluated from the following relationships: $Nb_L = \phi_{gc}Nb_{gc} + \phi_sNb_s$ and $\phi_{gc} + \phi_s = 1$. $Nb_L$ is the fitted scattering length density of the layer, $Nb_{gc}$ and $Nb_s$ are the theoretical scattering length densities of the gold core and of the solvent, respectively, and $\phi_{gc}$ and $\phi_s$ are the volume fractions of the gold core and the solvent, respectively. For the range of surface coverage studied, $\phi_{gc}$ varies from ~0.04 to 0.12.

When the temperature is increased from 20 to 30 °C (at $a \approx 100$ nm$^2$ per nanoparticle), a small increase in volume fraction is obtained, $\phi_{gc} \approx 0.15$, indicative of lateral contraction of the graft polymer layer. Taking the gold core density, $\rho = 19.3$ g/cm$^3$, the surface concentration in mg/m$^2$ can be evaluated from $\Gamma = \phi_{gc}\, d\rho \times 10^{-1}$.

Note that, in this series of experiments, the contrast between air and the gold-core ($\Delta Nb = -4.5 \times 10^{-6}$ Å$^{-2}$) is much higher than that between air and polymer/solvent ($\Delta Nb = -0.82 \times 10^{-6}$ Å$^{-2}$). Under these contrast conditions, reflectivity at the air-monolayer interface is dominated by the gold-core, with minimal sensitivity to any existence of an upper layer of adsorbed polymer/solvent (see next section). Furthermore, due to the limited $q$-range, possible staggering of the gold-cores cannot be measured directly; rather, these effects are implicit in the inclusion of interfacial roughness, $\sigma$. As mentioned above, due to the low signals, we have decided to fix the values of the interfacial roughness and limit the fitting parameters to only the volume fraction and thickness of the gold-core layer. The density profile thus results in an apparent shift of the interface toward the gold-core layer, neglecting the adsorbed polymer layer ($L_1$) discussed in the next section. This series of experiments is therefore sensitive to the structure of the gold-core layer but not to the exact location of its interface with respect to the air−liquid interface. Information on the position (with respect to the free surface) and staggering of gold-core can be better accessed by X-ray reflectivity, and these experiments are planned for future studies.

***2. Polymer Reflectivity.*** This series of experiments uses pure $D_2O$ as solvent in order to maximize the contrast between polymer and solvent, where $\Delta Nb = Nb_p - Nb_s = (0.90 - 6.39) \times 10^{-6}$ Å$^{-2}$ $= -5.49 \times 10^{-6}$ Å$^{-2}$. The gold core contributes to a much lesser extent due to its lower contrast with the solvent ($\Delta Nb = Nb_{gc} - Nb_s = (4.50 - 6.39) \times 10^{-6}$ Å$^{-2}$ $= -1.89 \times 10^{-6}$ Å$^{-2}$). It is, nevertheless, taken into account in the evaluation of the polymer density profile as described below. In this series, $R_F$ is the reflectivity of pure $D_2O$ and all deviations of $R/R_F$ from unity are attributed to the presence of the monolayer. In this case, due to the negative sign of $\Delta Nb$, $R/R_F < 1$.

*(a) Concentration Effects.* We find that, for this series of experiments where the reflectivity signal arises principally from the polymer, a single-layer profile is inadequate for fitting the data. The reflectivity spectra are fitted with an $n$-layer density profile described by

$$Nb(z) = \sum_0^n \left(\frac{Nb_i - Nb_{i+1}}{2}\right)\left(1 - \mathrm{erf}\frac{(z - z_i)}{\sigma_i}\right)$$

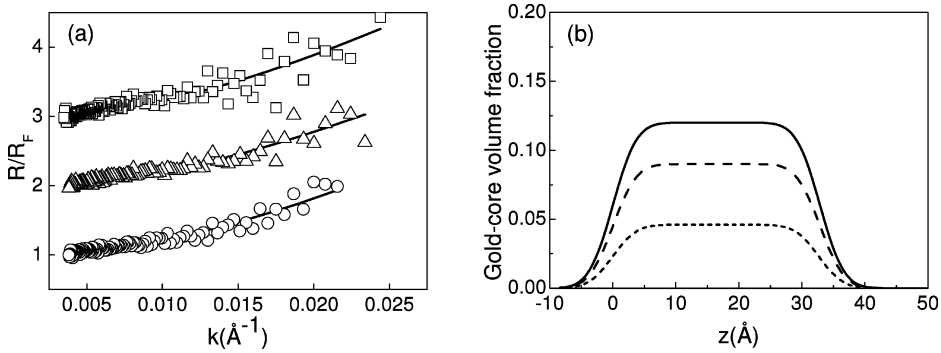


**Figure 3.** (a) Normalized reflectivity of the gold-core of PNIPAM-AuNP monolayer (the polymer is contrast-matched to solvent). The curves are vertically separated for better visualization. Surface coverage in area/nanoparticle: $a \approx 600$ nm$^2$ (circles, $y$-axis $= R/R_F$), $a \approx 200$ nm$^2$ (triangles, $y$-axis $= R/R_F + 1$), $a \approx 100$ nm$^2$ (squares, $y$-axis $= R/R_F + 2$). The solid lines are best-fit curves calculated with the corresponding particle density profiles shown in the figure (b): $a \approx 600$ nm$^2$ (dotted line), $a \approx 200$ nm$^2$ (dashed line), $a \approx 100$ nm$^2$ (solid line) per nanoparticle; $T = 20$ °C.

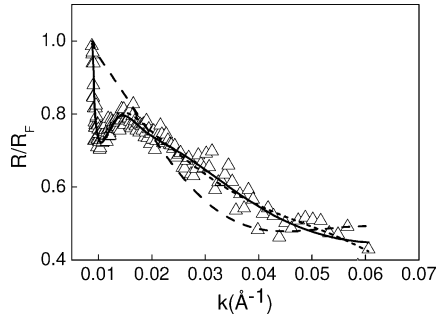


**Figure 4.** Normalized reflectivity of PNIPAM-AuNP monolayer on $D_2O$, showing a comparison of different fitted models: one-layer model (dashed line, $\chi^2 = 2.4583$); two-layer model (dotted line, $\chi^2 = 0.38801$); three-layer model (solid line, $\chi^2 = 0.37875$). Surface coverage $a \approx 200$ nm$^2$/nanoparticle, $T = 20$ °C.

$Nb_i$ is the scattering length density in layer $i$ with corresponding thickness $h_i = z_i - z_{i+1}$, and $\sigma_i$ is the interfacial roughness at each layer defined by an error-function. The data are fitted with different models consisting of an incremental number of layers, and the best-fit model is determined by the least-squares method.

Figure 4 compares the different models used to fit the data. Here, the inadequacy of a one-layer model for fitting the reflectivity data can already be noted visually; in this case, $\chi^2 = 2.4583$. A two-layer model gives a significantly better fit, an improvement easily discernible by eye, with $\chi^2 = 0.38801$. On the other hand, the difference between a two- and a three-layer model can no longer be distinguished visually, although the three-layer model yields a lower $\chi^2$ value, $\chi^2 = 0.37875$. A further increase in the number of layers does not improve the quality of the fit: four-layer model ($\chi^2 = 0.38187$); five-layer model ($\chi^2 = 0.74363$); six-layer model ($\chi^2 = 0.71022$). We thus rely solely on the $\chi^2$ values for the goodness of fit.

Figure 5a shows $R/R_F$ as a function of surface concentration ranging from $a \approx 600$ nm$^2$ to $a \approx 100$ nm$^2$/nanoparticle at $T = 20$ °C. The continuous lines are best-fit curves with corresponding density profiles shown in Figure 5b. It is found that, with the exception of the lowest concentration ($a \approx 600$ nm$^2$/nanoparticle), a three-layer model consistently gives the best-fit results. In interpreting this model, we adopt the following reasoning: the first layer ($L_1$) consists of adsorbed polymer that anchors the nanoparticle to the surface; the second layer ($L_2$) comprises the gold core + polymer; the third layer ($L_3$) consists of immersed chains and solvent in the subphase. From these considerations, the volume fractions of polymer in $L_1$ and $L_3$ are deduced from the following relations: $Nb_{L_i} = \phi_p Nb_p + \phi_{D_2O} Nb_{D_2O}$ and $\phi_p + \phi_{D_2O} = 1$, where $Nb_{L_i}$ is the fitted scattering length density in layer $i$. On the other hand, $L_2$ is considered to be a three-component layer and the polymer volume fraction is thus deduced from $Nb_L = \phi_p Nb_p + \phi_{D_2O} Nb_{D_2O} + \phi_{gc} Nb_{gc}$ and $\phi_p + \phi_{D_2O} + \phi_{gc} = 1$. $\phi_{gc}$ is the volume fraction of the gold core deduced from the first series of experiments where the polymer is contrast-matched to the solvent.

The polymer density profiles from Figure 5b show that, for all surface concentrations, the interfacial layer is characterized by a polymer-rich layer ($L_1$). The thickness of this layer increases from about ≈14 to ≈50 Å with a slight decrease in polymer volume fraction from $\phi_p \approx 0.98$ to 0.91.

The most interesting change in the polymer density profile is the appearance of the third (tail) layer, $L_3$, at $a \approx 200$ nm$^2$/nanoparticle, an area that corresponds approximately to the region of the second pressure rise ($A_b$) in the compression isotherm in Figure 1a. With further increase in nanoparticle concentration, $L_3$ increases in thickness and in polymer volume fraction. $\phi_p(z)$ in this layer decreases smoothly toward the bulk phase in a manner very similar to that observed for polymer brushes, commonly modeled by parabolic profiles.[33,34] In the present case, the smooth curve is a Gaussian error function that describes the roughness between $L_3$ and the bulk phase.

The increase in $L_3$ of the polymer density profile is accompanied by a dip in the second layer $L_2$ that in this model constitutes the composite layer containing the gold core. This apparent depletion zone suggests that the graft polymer chains are mostly either adsorbed or desorbed to form the brush structure in $L_3$. Note also that the thickness of $L_2$ is larger than the size of the gold core. This may be attributed in part to contribution of the gold−thiol linkage layer and, more probably, to staggering of the nanoparticles, thus increasing the effective thickness of this zone. Such staggering is not measurable in the first series (gold-core reflectivity) due to the lower gold core−solvent contrast and particle concentration and also to the small size of the gold core in view of the limited $q$-range. The much higher polymer−solvent contrast in this series thus permits a more precise determination of the polymer density profile.

*(b) Temperature Effects.* An increase in temperature decreases solvent quality for PNIPAM, resulting in modifications in the structure of the polymer layer. Figure 6a shows $R/R_F$ at $a \approx 100$ nm$^2$ per nanoparticle for $T = 20$ °C, 25 and 30 °C. The corresponding fitted concentration profiles are shown in Figure 6b. The profiles show a very clear progressive decrease in $L_3$. Similar contractions can also be seen in $L_1$. Contractions of these two zones are accompanied by an increase in the segment density in $L_2$.

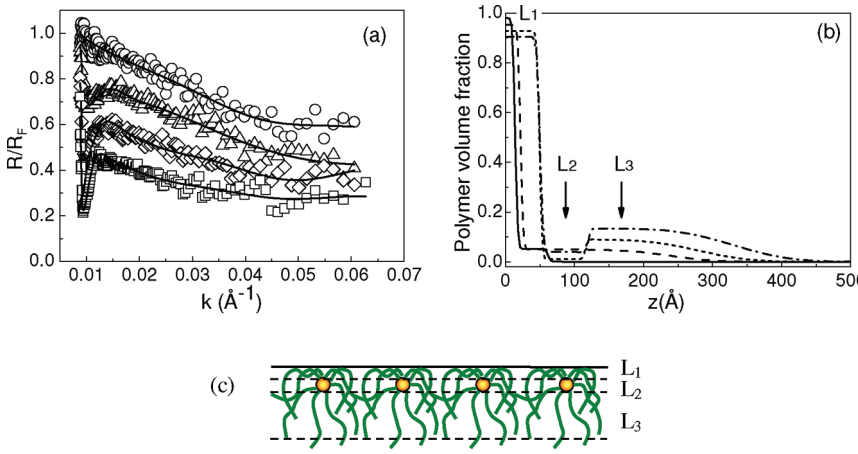


**Figure 5.** (a) Normalized reflectivity of PNIPAM-AuNP monolayer on $D_2O$ at different surface coverage; $T = 20$ °C. The reflectivity signals are due mainly to the polymer. The spectra are vertically separated by a factor $f$ for better visualization. Surface coverage in area/nanoparticle: $a \approx 600$ nm$^2$ (circles, $f = 1$), $a \approx 200$ nm$^2$ (triangles, $f = 0.95$), $a \approx 120$ nm$^2$ (diamonds, $f = 0.8$), $a \approx 100$ nm$^2$ (squares, $f = 0.7$). The solid lines are best-fit curves calculated with the corresponding polymer density profiles shown in part b: $a \approx 600$ nm$^2$ (solid line), $a \approx 200$ nm$^2$ (dashed line), $a \approx 120$ nm$^2$ (dotted line), $a \approx 100$ nm$^2$ (dot-dashed line). (c) Schematic diagram of the three-layer model.

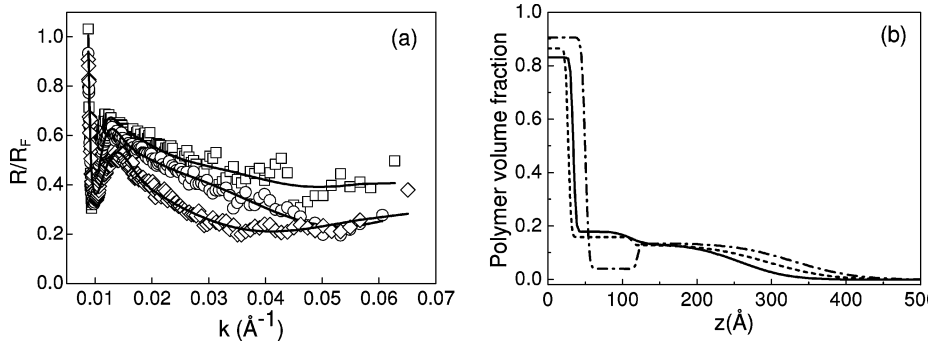


**Figure 6.** Effect of temperature on PNIPAM-AuNP monolayer on $D_2O$. The reflectivity signals are due mainly to the polymer. (a) Normalized reflectivity at $T = 20$ °C (squares), $T = 25$ °C (circles), or $T = 30$ °C (diamonds). The solid lines are best-fit curves calculated with the corresponding polymer density profiles shown in part b: $T = 20$ °C (dot-dashed line), $T = 25$ °C (dotted line), or $T = 30$ °C (solid line); $a \approx 100$ nm$^2$ per nanoparticle.

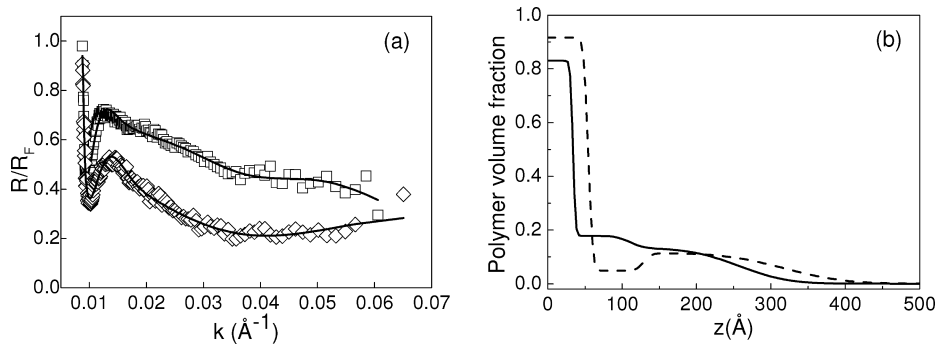


**Figure 7.** Reversibility of contraction−expansion of PNIPAM-AuNP monolayer. (a) Normalized reflectivity: $T = 30$ °C (open diamonds); cooled down to $T = 20$ °C (open squares). The solid lines are best-fit curves calculated with the corresponding polymer density profiles shown in part b: $T = 30$ °C (solid line); cooled down to 20 °C (dashed line).

We point out that these temperature-induced contractions are not always observable. In the case of adsorbed PNIPAM homopolymer, for example, a decrease in solvent quality promotes intermolecular attraction that leads to multilayer formation, resulting in a significant increase in thickness of the interfacial layer.[32] For the PNIPAM-AuNP system in the present study, significant interparticle aggregation is prevented by the carboxyl end groups of the cpa-RAFT agent used in the polymer synthesis.

*(c) Reversibility of Brush Contraction−Expansion.* Reversibility of the thermal response of the monolayer is studied by heating−cooling cycles. Figure 7 shows that, upon cooling the sample from $T = 30$ °C to $T = 20$ °C, both $L_3$ and $L_1$ increase in thickness. Thus, the contracted monolayer recovers its expanded structures when cooled to good-solvent condition. Furthermore, the contraction−expansion of the polymer layer can be reproduced through several heating−cooling cycles, showing the good thermal stability of the monolayer (between 20° and 30 °C).

The two series of neutron reflectivity experiments presented above are thus designed to access separately information on the gold-core and on the graft polymer layers. These complementary pieces of information yield detailed structural characterizations of the composite nanoparticle monolayer and their

**TABLE 1: Fitted Parameters for Gold-Core Reflectivity of PNIPAM-AuNP Monolayers (Polymer Contrast-Matched to Solvent)**

| $T$ (°C) | area/nanoparticle ($nm^2$) | $d$ (Å) | Nb × $10^6$ ($Å^{-2}$) | $\phi_{gc}$ | $\Gamma_{gc}$ ($mg/m^2$) |
|---|---|---|---|---|---|
| 20 | 600 | 32.7 | 1.00 | 0.046 | 2.90 |
| 20 | 300 | 32.8 | 1.10 | 0.076 | 4.81 |
| 20 | 200 | 32.9 | 1.15 | 0.090 | 5.71 |
| 20 | 120 | 33.9 | 1.13 | 0.084 | 5.44 |
| 20 | 100 | 32.9 | 1.26 | 0.120 | 7.62 |
| 30 | 100 | 33.4 | 1.37 | 0.150 | 9.67 |

**TABLE 2: Fitted Parameters for Polymer Reflectivity of PNIPAM-AuNP Monolayers from $D_2O$**

| $T$ | area/nanoparticle ($nm^2$) | | thickness (Å) | Nb × $10^6$ ($Å^{-2}$) | $\phi_p$ | $\Gamma_p$ ($mg/m^2$) |
|---|---|---|---|---|---|---|
| 20 | 600 | $L_1$ | 14.1 | 1.00 | 0.982 | 1.48 |
| | | $L_2$ | 47.5 | 6.01 | 0.055 | 0.28 |
| | | $L_3$ | 20.1 | 6.37 | ~0 | 0 |
| | | | | | | Total = 1.76 |
| 20 | 200 | $L_1$ | 21.8 | 1.16 | 0.952 | 2.22 |
| | | $L_2$ | 76.9 | 6.04 | 0.051 | 0.42 |
| | | $L_3$ | 140.3 | 6.12 | 0.049 | 0.74 |
| | | | | | | Total = 3.38 |
| 20 | 120 | $L_1$ | 49.4 | 1.29 | 0.928 | 4.91 |
| | | $L_2$ | 66.2 | 6.20 | 0.011 | 0.08 |
| | | $L_3$ | 164.5 | 5.85 | 0.090 | 1.59 |
| | | | | | | Total = 6.57 |
| 20 | 100 | $L_1$ | 50.1 | 1.41 | 0.905 | 4.85 |
| | | $L_2$ | 70.1 | 5.95 | 0.057 | 0.29 |
| | | $L_3$ | 210.1 | 5.54 | 0.134 | 3.02 |
| | | | | | | Total = 8.17 |
| 25 | 100 | $L_1$ | 27.1 | 1.63 | 0.864 | 2.51 |
| | | $L_2$ | 85.9 | 5.32 | 0.158 | 1.45 |
| | | $L_3$ | 182.3 | 5.57 | 0.129 | 2.51 |
| | | | | | | Total = 6.47 |
| 30 | 100 | $L_1$ | 34.0 | 1.81 | 0.830 | 3.02 |
| | | $L_2$ | 76.5 | 5.19 | 0.178 | 1.46 |
| | | $L_3$ | 146.5 | 5.55 | 0.132 | 2.08 |
| | | | | | | Total = 6.56 |
| 20 | 100 | $L_1$ | 54.5 | 1.35 | 0.916 | 5.34 |
| | cooled down | $L_2$ | 74.5 | 5.91 | 0.049 | 0.39 |
| | from 30 °C | $L_3$ | 190.3 | 5.66 | 0.114 | 2.31 |
| | | | | | | Total = 8.04 |

responses to compression and temperature. The fitted parameters are given in Tables 1 and 2.

Figure 8 compares the surface density of the nanoparticles evaluated from reflectivity experiments with the calculated initial amount deposited. These results show good agreement between experimental and calculated values, showing the acceptable spreading coefficient of the nanoparticles spread from chloroform using the incremental drop method.

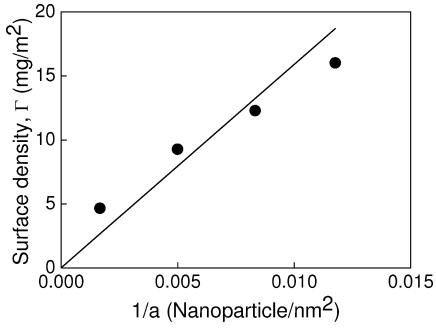


**Figure 8.** Comparison of the PNIPAM-AuNP surface density (gold-core + grafted polymer layer) evaluated from neutron reflectivity (circles) with the amount deposited (solid line).

## Discussion

**PNIPAM as a Surface-Active Agent.** PNIPAM is among the most surface-active water-soluble polymers. It adsorbs spontaneously at the water−air interface, reducing the interfacial tension to about 40 mN $m^{-1}$. Hydrophilic nanoparticles can thus be rendered surface-active when coated with a layer of PNIPAM. This has been shown for the case of PNIPAM-activated adsorption of charged silica nanoparticles at the water−air interface.[35] Similarly, gold nanoparticles protected by graft PNIPAM chains are rendered colloidally stable and amphiphilic. These composite PNIPAM-AuNPs can therefore be spread on the water surface to form stable Langmuir monolayers where their structural properties can be modulated by isothermal compression and by temperature.

**Compression-Induced Conformational Changes.** That stable monolayers can be formed with PNIPAM-AuNPs without additional anchoring agents is an attribute of the highly surface-active nature of PNIPAM. The compression isotherm shows a low-pressure rise region that yields a limiting area of $A_p \approx 1250$ $nm^2$ per nanoparticle, generally designated as the limiting pancake area where the polymer chains are adsorbed in a flat conformation. At increased surface coverage, a pseudoplateau is obtained followed by a second pressure rise region that gives a limiting area of $A_b \approx 200-300$ $nm^2$ per nanoparticle. This second limiting area is often considered to indicate a conformational transition to a brush structure, and the pseudoplateau thus represents a region of coexistence of pancake−brush structures. This interpretation however is debatable, in particular for monolayers tethered to the surface by insoluble blocks that at high compression can interact and cause the pressure rise. Qualitatively, the PNIPAM-AuNP compression isotherm resembles that for adsorbed PNIPAM homopolymer, indicating that the interfacial behavior of PNIPAM-AuNP is dominated by the graft PNIPAM chains. However, two differences are noted in the PNIPAM-AuNP isotherm: the steeper slope of the pseudoplateau, and a second pressure rise at $A_b \approx 200-300$ $nm^2$ (absent for PNIPAM homopolymer), suggesting a higher degree of structural reorganization in the PNIPAM-AuNP layer. The nanoparticle monolayer remains stable up to about ~100 $nm^2$ per nanoparticle.

Contrast-matched neutron reflectivity measurements from this study reveal detailed structure and organization of the nanocomposite monolayer. Three distinct zones/layers describe the monolayer structure: the first layer ($L_1$) consists of adsorbed polymer segments that anchor the nanoparticle to the surface, the second layer ($L_2$) constitutes the zone where the gold-core resides, and the third layer ($L_3$) comprises polymer chains submerged in the solvent subphase. $L_1$ (air-side) is polymer-rich and $L_3$ solvent-rich.

Upon compression, several notable changes in the polymer density profile can be seen. The first is the development of $L_3$, which increases in thickness and in polymer volume fraction. This feature is characteristic of formation of brushlike structures. In conjunction with the brush formation, the polymer-rich adsorbed layer ($L_1$) increases in thickness from 25−30 Å to about 50 Å. Interestingly, as $L_1$ and $L_3$ grow in thickness and in polymer concentration, the middle gold-core layer ($L_2$) remains polymer-poor (<10% by volume of polymer) with the appearance of a depletion zone. Thus, as surface coverage increases, the polymer segments are pushed out of $L_2$, and two distinct conformational structures coexist: adsorbed conformation and stretched brushlike structure. The former is characterized by a thin and compact layer that anchors the nanoparticles to the surface, and the latter by a dilute extended brush layer.

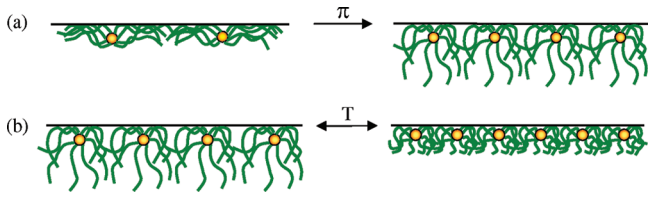


**Figure 9.** Schematic representations of conformational changes of PNIPAM-AuNP monolayers: (a) compression-induced pancake-to-brush transition, (b) reversible temperature-induced contraction−expansion of polymer-graft layer and modulation of interparticle distance.

**Thermally Induced Conformational Changes.** The most interesting feature of the PNIPAM-AuNPs lies in their thermal response. Past studies using neutron scattering[36] and reflectivity[32,37] have revealed a temperature-induced expansion−collapse transition of PNIPAM chains in bulk as well as at the surface. In the present study, we show that PNIPAM chains grafted onto nanoparticles also undergo similar expansion−collapse at the interface. When the temperature is increased from 20 to 30 °C, while compression isotherms indicate only very small changes, neutron reflectivity data reveal clear and significant changes in the conformation of the grafted chains. Here, both adsorbed ($L_1$) and brush ($L_3$) polymer layers are shown to exhibit significant contractions due to decreased solvent quality (Θ-temperature ~29 °C), with a concomitant increase in polymer density in $L_2$. These conformational changes are accompanied by a decrease in interparticle distance, indicating lateral contraction of the polymer graft layer. We point out that such monolayer contractions are not always observable, since a decrease in solvent quality promotes intermolecular attraction that leads to multilayer formation and a significant increase in layer thickness.[32] In the case of a PNIPAM-AuNP monolayer, preservation of the unilayer structure is assured by the presence of charged end-groups on the polymer chains, as mentioned in the Experimental Section.

The attractive aspect of a thermosensitive system lies not only in the ease with which temperature can be used to stimulate a rapid response in the polymer conformation. The reversibility of this action is equally desirable. This aspect is clearly demonstrated by the reversible contraction−expansion of the polymer layers by heating−cooling cycles.

At the interface, therefore, the thermosensitive nature of PNIPAM chains grafted onto the nanoparticle undergoes similar thermally induced expansion−collapse. The graft PNIPAM layer can thus act as a reversible thermoswitch to modulate interparticle distance and the chemical environment of the gold-core layer (see Figure 9).

**Relation of Conformational Changes to Optical Properties.** An interesting aspect of the gold nanoparticle Langmuir monolayer is its optical properties—as in bulk solution, these interfacial nanoparticles exhibit surface plasmon resonance. Past studies have reported the possibility to tune the optical properties of the monolayer by surface compression.[38,39] In these studies, changes in optical properties (red-shift) have mostly been attributed to a decrease in interparticle distances. However, a recent report shows, interestingly, that very small particles are sensitive to nonlocal effects that are enhanced with decreasing interparticle distance, resulting in an optical blue-shift instead of the expected red-shift.[40]

For polymer-coated nanoparticles, the presence of the polymer layer and changes in conformation of the polymer chains can also affect optical properties. This is shown in the Mie−Drude theory:[5,14,15]

$$\lambda_{peak} = \lambda_p \sqrt{\varepsilon^{\infty} + 2\varepsilon_m + \frac{2g(\varepsilon_s - \varepsilon_m)}{3}}$$

where $\lambda_{peak}$ is the absorption peak position for the nanoparticle and $\lambda_p$ the bulk plasma wavelength. $\varepsilon^{\infty}$, $\varepsilon_s$, and $\varepsilon_m$ are dielectric functions of the bulk metal, polymer shell layer and medium, respectively; g is the volume fraction of the polymer shell layer. Two points can be noted from the above equation: (i) since $\varepsilon_s > \varepsilon_m$ for most polymers in aqueous medium, the presence of a polymer shell layer increases $\lambda_{peak}$ with respect to the naked nanoparticle ($g = 0$), and (ii) since $(\varepsilon_s - \varepsilon_m)$ is concentration-dependent, $\lambda_{peak}$ is therefore also sensitive to the polymer conformation.

We have shown that, upon compression of the PNIPAM-Au nanoparticle Langmuir monolayer, interparticle distance decreases, with an accompanying change in conformation of the graft polymer layer. In particular, adsorbed polymer chains are partially displaced to form brush structures. Changes in polymer conformation can further be modulated by temperature, as shown by the reversible collapse−expansion of the polymer layer by heating−cooling cycles. These modifications in polymer structure can thus be expected to affect the term $(\varepsilon_s - \varepsilon_m)$ and therefore the optical properties of the nanoparticles, as shown in a recent report for gold nanoparticles encapsulated with PNIPAM microgel.[25]

## Conclusions

Amphiphilic PNIPAM-Au nanoparticles form stable Langmuir monolayers that exhibit surface plasmon resonance. The structures of the monolayers and their changes induced by isothermal compression and by temperature have been revealed by contrast-matched neutron reflectivity studies. These results show that, at low surface concentration, the gold nanoparticles are attached to the surface by PNIPAM chains adsorbed in a pancake conformation forming a thin and compact layer. Upon isothermal compression to higher surface coverage, these adsorbed chains are partially desorbed from the surface to form brush structures immersed in the bulk phase, with a depletion zone between the adsorbed and brush layers. Coexistence of brush structures with adsorbed chains that anchor the nanoparticles to the surface explains the stability of the monolayer without additional hydrophobic anchoring agents. With increase in temperature, the PNIPAM graft layer contracts with a concomitant decrease in interparticle distance. The reversibility of this contraction is demonstrated by the contraction−expansion of the polymer layer in heating−cooling cycles. A graft PNIPAM layer can thus be used as a potential reversible thermoswitch to modulate interparticle distance and the dielectric environment of gold nanoparticle monolayers. This opens the possibility to tune optical properties of nanoparticle monolayers by two convenient levers, such as compression and temperature.

**Acknowledgment.** We thank F. Cousin and A. Menelle for their help in ensuring smooth functioning of the neutron reflectometer, and N. Del Fatti and F. Vallée for discussions on optical properties.

## References and Notes

(1) The British Museum (www.thebritishmuseum.ac.uk/science/text/lycurgus/sr-lycurgus-pl-t.html).
(2) Faraday, M. *Philos. Trans. R. Soc. London* **1857**, *147*, 145.
(3) Henglein, A. *Chem. Rev.* **1989**, *89*, 1861.
(4) Hayat, M. A., Ed. Colloid Gold: Principles, Methods, and Applications; Academic Press: San Diego, CA, 1989; Vol. 1.

(5) Kreibig, U.; Vollmer, M. *Optical Properties of Metal Clusters*; Springer: Berlin, 1995.
(6) Shipway, A. N.; Katz, E.; Willner, I. *ChemPhysChem* **2000**, *1*, 18.
(7) Johnston, R. L. *Atomic and Molecular Clusters*; Taylor & Francis: London, 2002.
(8) Doremus, R. H. *J. Chem. Phys.* **1964**, *40*, 2389.
(9) Alvarez, M. M.; Khoury, J. T.; Schaft, T. G.; Shafigullen, M. N.; Vezmar, I.; Whetten, R. L. *J. Phys. Chem. B* **1997**, *101*, 3706.
(10) Palpant, B.; Prével, B.; Lermé, J.; Cottancin, E.; Pellarin, M.; Treilleux, M.; Perez, A.; Vialle, J. L.; Broyer, M. *Phys. Rev. B* **1998**, *57*, 1963.
(11) Link, S.; El-Sayed, M. A. *J. Phys. Chem. B* **1999**, *103*, 4212.
(12) (a) Liz-Marzan, L. M. *Langmuir* **2006**, *22*, 32. (b) Ung, T.; Liz-Marzan, L. M.; Mulvaney, P. *J. Phys. Chem. B* **2001**, *105*, 3441.
(13) Kelly, K. L.; Coronado, E.; Zhao, L. L.; Schatz, G. C. *J. Phys. Chem. B* **2003**, *107*, 668.
(14) Mulvaney, P. *Langmuir* **1996**, *12*, 788.
(15) Templeton, A. C.; Pietron, J. J.; Murray, R. W.; Mulvaney, P. *J. Phys. Chem. B* **2000**, *104*, 564.
(16) Yamada, M.; Tadera, T.; Kubo, K.; Nishihara, H. *Langmuir* **2001**, *17*, 2363.
(17) Morones, J. R.; Frey, W. *Langmuir* **2007**, *23*, 8180.
(18) Malikova, N.; Pastoriza-Santos, I.; Schierhorn, M.; Kotov, N. A.; Liz-Marzán, L. M. *Langmuir* **2002**, *18*, 3694.
(19) Jiang, C.; Markutsya, S.; Tsukruk, V. V. *Langmuir* **2004**, *20*, 882.
(20) Srivastava, S.; Frankamp, B. L.; Rotello, V. M. *Chem. Mater.* **2005**, *17*, 487.
(21) Raula, J.; Shan, J.; Nuopponen, M.; Niskanen, A.; Jiang, H.; Kauppinen, E. I.; Tenhu, H. *Langmuir* **2003**, *19*, 3499.
(22) Shan, J.; Nuopponen, M.; Jiang, H.; Kauppinen, E.; Tenhu, H. *Macromolecules* **2003**, *36*, 4526.
(23) Shan, J.; Nuopponen, M.; Jiang, H.; Viitala, T.; Kauppinen, E.; Kontturi, K.; Tenhu, H. *Macromolecules* **2005**, *38*, 2918.
(24) Shan, J.; Chen, J.; Nuopponen, M.; Viitala, T.; Jiang, H.; Peltonen, J.; Kauppinen, E.; Tenhu, H. *Langmuir* **2006**, *22*, 794.
(25) Contreras-Caceres, R.; Sanchez-Iglesias, A.; Karg, M.; Pastoriza-Santos, I.; Perez-Juste, J.; Pacifica, J.; Hellweg, T.; Fernandez-Barbero, A.; Liz-Marzin, L. M. *Adv. Mater.* **2008**, *20*, 1666.
(26) Ganachaud, F.; Monteiro, M. J.; Gilbert, R. G.; Dourges, M.-A.; Thang, S. H.; Rizzardo, E. *Macromolecules* **2000**, *33*, 6738.
(27) Born, M.; Wolf, E. *Principles of Optics*; Pergamon: Oxford, 1975.
(28) Crowley, T. L.; Lee, E. M.; Simister, E. A.; Thomas, R. K.; Penfold, J.; Rennie, A. R. *Colloids Surf.* **1990**, *52*, 85.
(29) Lee, L. T.; Mann, E. K.; Guiselin, O.; Langevin, D.; Farnoux, B.; Penfold, J. *Macromolecules* **1993**, *26*, 7046.
(30) Lee, L. T.; Langevin, D.; Mann, E. K.; Farnoux, B. *Physica B* **1994**, *198*, 83.
(31) Bijsterbosch, H. D.; de Haan, V. O.; de Graaf, A. W.; Mellema, M.; Leermakers, F. A. M.; Cohen Stuart, M. A.; van Well, A. A. *Langmuir* **1995**, *11*, 4467.
(32) Lee, L. T.; Jean, B.; Menelle, A. *Langmuir* **1999**, *15*, 3267.
(33) Kent, M. S.; Lee, L. T.; Farnoux, B.; Rondelez, F. *Macromolecules* **1992**, *25*, 6240.
(34) Kent, M. S.; Majewski, J.; Smith, G. S.; Lee, L. T.; Satija, S. *J. Chem. Phys.* **1998**, *108*, 5635.
(35) Rezende, C. A.; Lee, L. T.; Galembeck, F. *Langmuir* **2008**, *24*, 7346.
(36) Lee, L. T.; Cabane, B. *Macromolecules* **1997**, *30*, 6559.
(37) Jean, B.; Lee, L. T.; Cabane, B. *Langmuir* **1999**, *15*, 7585.
(38) Heath, J. R.; Knobler, C. M.; Leff, D. V. *J. Phys. Chem. B* **1997**, *101*, 189.
(39) Liljeroth, P.; Vanmaekelbergh, D.; Ruiz, V.; Kontturi, K.; Jiang, H.; Kauppinen, E.; Quinn, B. M. *J. Am. Chem. Soc.* **2004**, *126*, 7126.
(40) Javier Garcia de Abajo, F. *J. Phys. Chem. C* **2008**, *112*, 17983.

JP9019393